




# Elastic study of electric quadrupolar correlation in the paramagnetic state of the frustrated quantum magnet $\text{Tb}_{2+\delta}\text{Ti}_{2-\delta}\text{O}_7$

Y. Nii <sup>1,2,\*</sup>, Y. Hirokane,<sup>3</sup> S. Nakamura,<sup>1</sup> N. Kabeya,<sup>4,5</sup> S. Kimura,<sup>1</sup> Y. Tomioka,<sup>6</sup> T. Nojima <sup>1</sup> and Y. Onose <sup>1</sup>

<sup>1</sup>*Institute for Materials Research, Tohoku University, Sendai 980-8577, Japan*

<sup>2</sup>*PRESTO, Japan Science and Technology Agency (JST), Kawaguchi 332-0012, Japan*

<sup>3</sup>*Department of Basic Science, University of Tokyo, Tokyo 153-8902, Japan*

<sup>4</sup>*Graduate School of Science, Tohoku University, Sendai 980-8578, Japan*

<sup>5</sup>*Center for Low Temperature Science, Tohoku University, Sendai 980-8578, Japan*

<sup>6</sup>*National Institute of Advanced Industrial Science and Technology (AIST), Tsukuba 305-8562, Japan*



(Received 24 September 2021; revised 21 January 2022; accepted 1 March 2022; published 10 March 2022)

The electric quadrupolar state in the frustrated quantum magnet  $\text{Tb}_{2+\delta}\text{Ti}_{2-\delta}\text{O}_7$  has been studied by means of ultrasonic and magnetostriction measurements. A single crystal showed an elastic anomaly around 0.4 K, manifesting a long-range quadrupole ordering. By investigating the anisotropy of the magnetoelastic responses, we found a crossover temperature for the strongly correlated quadrupole state, below which the experimental data of the elastic constant and magnetostriction become qualitatively different from their calculations based on a single-ion model. We suppose that relatively high onset temperature of the quadrupole correlation compared with the transition temperature is ascribed to the geometrical frustration effect, and this correlated state seems to be responsible for the unusual properties in the paramagnetic state of  $\text{Tb}_2\text{Ti}_2\text{O}_7$ .

DOI: [10.1103/PhysRevB.105.094414](https://doi.org/10.1103/PhysRevB.105.094414)

## I. INTRODUCTION

Geometrically frustrated systems have been serving as a fertile playground for studying nontrivial magnetic phenomena [1,2]. The pyrochlore lattice is a prototypical structure having geometrical frustration, where conventional magnetic order fails to develop and nontrivial states often emerge. In particular,  $\text{Dy}_2\text{Ti}_2\text{O}_7$  and  $\text{Ho}_2\text{Ti}_2\text{O}_7$  exhibit a novel phenomenon of spin ice, in which magnetic moments remain disordered down to the lowest temperature, showing a zero-point entropy [3]. The dynamics of magnetic monopoles under magnetic fields have also attracted much attention [4]. Distinct from these classical Ising spin systems, the presence of quantum fluctuations, or transverse interaction, in systems with weaker magnetic anisotropy provides more exotic physics related to the quantum spin liquid (QSL) state in the ground state [5–7]. In quests of such quantum spin ice systems, intensive studies have been performed [8–10] based on compounds of  $\text{Yb}_2\text{Ti}_2\text{O}_7$ ,  $\text{Er}_2\text{Ti}_2\text{O}_7$ ,  $\text{Tb}_2\text{Ti}_2\text{O}_7$ ,  $\text{Pr}_2\text{Zr}_2\text{O}_7$ , and so on.

Among them,  $\text{Tb}_2\text{Ti}_2\text{O}_7$  shows unique magnetic properties with  $\text{Tb}^{3+}$  ions having a total angular momentum  $J = 6$ . The trigonal crystalline electric field (CEF) partially lifts the degeneracy, and produces a low energy level scheme, that consists of the ground state doublet and first excited doublet separated only by  $\approx 18$  K [11]. The small gap allows admixing between them, and quantum fluctuation transverse to their local Ising axis becomes important [5,6,12]. This

material has been thought of as a candidate of QSL. Despite a negative Curie-Weiss temperature of  $\Theta_{CW} = -19$  K [8,13], no magnetic long-range order was observed down to the achievable lowest temperatures [13,14], while short-range magnetic correlation develops below several tens of kelvins as revealed by various methods:  $\mu\text{SR}$  [11,15], AC susceptibility [14,16], neutron spin echo [14,17], and diffuse neutron scattering [18–22] suggested the characteristic magnetic state often referred to as a cooperative (or correlated) paramagnet [13]. In addition to a magnetic dipole moment, these doublets carry a large electric quadrupolar moment, which couples to local strain. Recently, quadrupole order has been discerned around 0.5 K [23,24] for Tb-rich  $\text{Tb}_{2+\delta}\text{Ti}_{2-\delta}\text{O}_7$  crystals. These findings imply that the quadrupolar moment plays an important role in this system; quadrupole moment  $O_\Gamma$  and strain  $e_\Gamma$  are linearly coupled by a quadrupole-strain coupling constant  $g_\Gamma$  ( $\Gamma$  represents an irreducible representation) as [25]

$$\mathcal{H}_{QS} = g_\Gamma O_\Gamma e_\Gamma. \quad (1)$$

$\text{Tb}_2\text{Ti}_2\text{O}_7$  shows prominent magnetoelastic responses such as significant elastic softening [24,26,27], giant magnetostriction [26,28,29], suppressed thermal conductivity [30], thermal Hall effect [31,32], and dynamical hybridization of phonon and crystalline electric field (CEF) states [33–35]. These experiments suggest that pure spin models are not enough to capture the physics of  $\text{Tb}_2\text{Ti}_2\text{O}_7$ , and the quadrupolar degree of freedom and its coupling to the lattice have to be considered carefully.

Here we have investigated the quadrupole correlation in Tb-rich  $\text{Tb}_{2+\delta}\text{Ti}_{2-\delta}\text{O}_7$  ( $\delta \approx 0.02$ ) by measuring the detailed temperature and magnetic field dependencies of the elastic

\*Corresponding author: yoichi.nii.c1@tohoku.ac.jp

constant and magnetostriction. The elastic constant [25] and the strain [36] are expressed as

$$C_{\Gamma} = C_{\Gamma}^0 - Ng_{\Gamma} \left. \frac{\partial \langle O_{\Gamma} \rangle}{\partial e_{\Gamma}} \right|_{e_{\Gamma}=0}, \quad (2)$$

$$e_{\Gamma} = \frac{Ng_{\Gamma}}{C_{\Gamma}} \langle O_{\Gamma} \rangle. \quad (3)$$

Here  $C_{\Gamma}^0$  is the elastic constant without considering quadrupole-strain coupling,  $\langle O_{\Gamma} \rangle$  represents statistical average of quadrupolar moment, and  $N$  is the number of Tb ions in a unit volume. These equations mean that two methods in this study are complementary and suitable for probing quadrupole fluctuation and quadrupole moment, respectively. By performing ultrasound measurement down to below 0.4 K, we have found a clear anomaly in elastic constant at the quadrupole ordering temperature of 0.44 K, being consistent with previous works [23,24]. We show strong quadrupolar correlation persists up to  $\approx 10$  K by comparing experimental data and calculation.

## II. EXPERIMENT

A single crystal of  $\text{Tb}_{2+\delta}\text{Ti}_{2-\delta}\text{O}_7$  was grown by the floating-zone method under 1 atm  $\text{O}_2$  atmosphere. The color of the single crystal is reddish brown. Laue photographs were used to determine the crystallographic orientation. X-ray diffractometer (XRD) measurements (SmartLab, Rigaku) were also performed to determine the lattice parameter. We also confirmed single-crystallinity and the absence of impurity phase in our sample by these measurements. The sample was cut and carefully polished to obtain rectangular shape with flat and parallel {100} surfaces. In order to characterize the sample, specific heat measurements were performed based on the quasiadiabatic method using a dilution refrigerator. We used the same piece of the single crystal as the ultrasonic measurement mentioned below, and focused on the low-temperature region at 0 T.

The size of the sample for ultrasonic measurements is  $4.2 \times 3.3 \times 1.7 \text{ mm}^3$ . Polyvinylidene difluoride (PVDF) films with thickness of  $9 \mu\text{m}$  were attached on (001) surfaces by room-temperature-vulcanizing (RTV) silicone. Longitudinal ultrasound of about 100 MHz is generated/detected by these PVDF transducers. Based on the pulse-echo method, an elastic constant of  $C_{11}$ , where both wave vector  $\mathbf{k}$  and polarization vector  $\mathbf{u}$  are parallel to [001], was obtained. Ultrasound echoes and reference signal were directly converted to digital data using an oscilloscope (RTO1004, Rohde & Schwarz), and phase comparison analysis was numerically performed. Note that magnetostriction of  $\text{Tb}_2\text{Ti}_2\text{O}_7$  was so large that adhesion between transducer and sample was easily broken under large magnetic fields when a hard transducer such as  $\text{LiNbO}_3$  was used. Therefore, we used the organic PVDF film that can be applicable even under large magnetostriction. Only the longitudinal mode is available for the PVDF transducer. Magnetostriction measurement was carried out by a conventional strain-gauge technique. We simultaneously measured longitudinal and transverse strains by orthogonally attaching two strain-gauges with external magnetic field applied along [001]. In order to eliminate false strain due to magnetore-

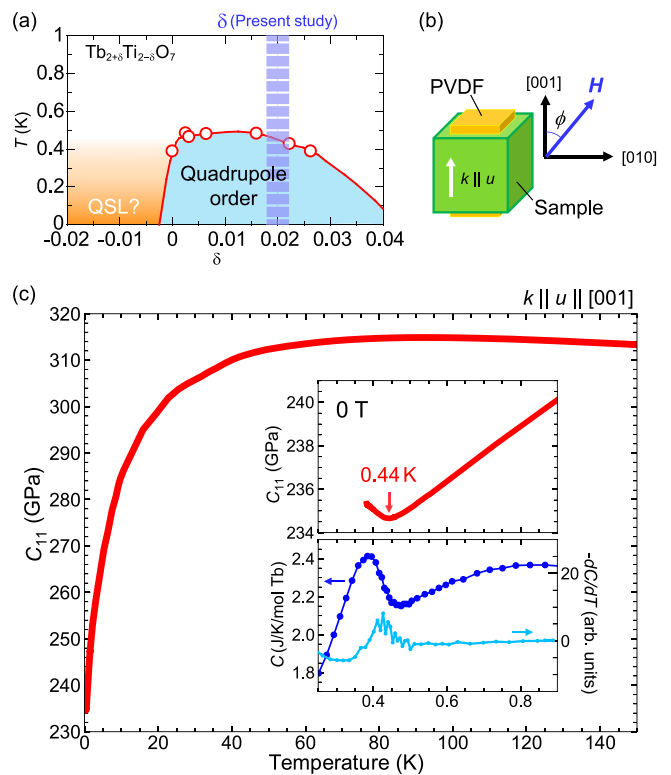


FIG. 1. (a)  $\delta$ - $T$  phase diagram of  $\text{Tb}_{2+\delta}\text{Ti}_{2-\delta}\text{O}_7$ . The composition of present study is estimated to  $\delta \approx 0.02$  based on XRD and specific heat measurements. Circles were data taken from Ref. [37]. (b) Experimental setup of ultrasound measurement. (c) Temperature dependence of compressive elastic constant  $C_{11}$  at 0 T. The insets show low-temperature region of  $C_{11}$  (top) and specific heat (bottom). Temperature derivative of the specific heat was also displayed in the bottom inset. Deflection of  $C_{11}$  at 0.44 K is close to the peak of  $-dC/dT$ , indicating the ordering of quadrupole moment.

sistance of strain gauge, a reference sample (glass) was also measured by the same settings. True magnetostriction was derived by subtracting the magnetoresistance from raw data. Ultrasonic measurement below 2 K was performed by using a  $^3\text{He}$  refrigerator at the Center for Low Temperature Science in Tohoku University. The lowest temperature achieved was 0.38 K. Detailed magnetic field angle dependence was measured above 2 K using a  $^4\text{He}$  refrigerator equipped with a rotation stage.

## III. RESULTS

As shown in Fig. 1(a), stoichiometric  $\text{Tb}_2\text{Ti}_2\text{O}_7$  locates close to the boundary of a QSL and a quadrupolar ordered phase, and the ground state is very sensitive to the off-stoichiometric parameter  $\delta$  [37,38]. As discussed below, our crystals seem to have  $\delta \approx 0.02$ . Therefore, the ground state may show a quadrupolar ordering. Figure 1(c) exhibits temperature dependence of compressive elastic constant  $C_{11}$ . Large elastic softening was observed with decreasing temperature followed by the hardening below 0.44 K. The softening is caused by quadrupole fluctuation while the hardening suggests that the ground state degeneracy was lifted by a phase transition. This upturn is consistent with the previous reports

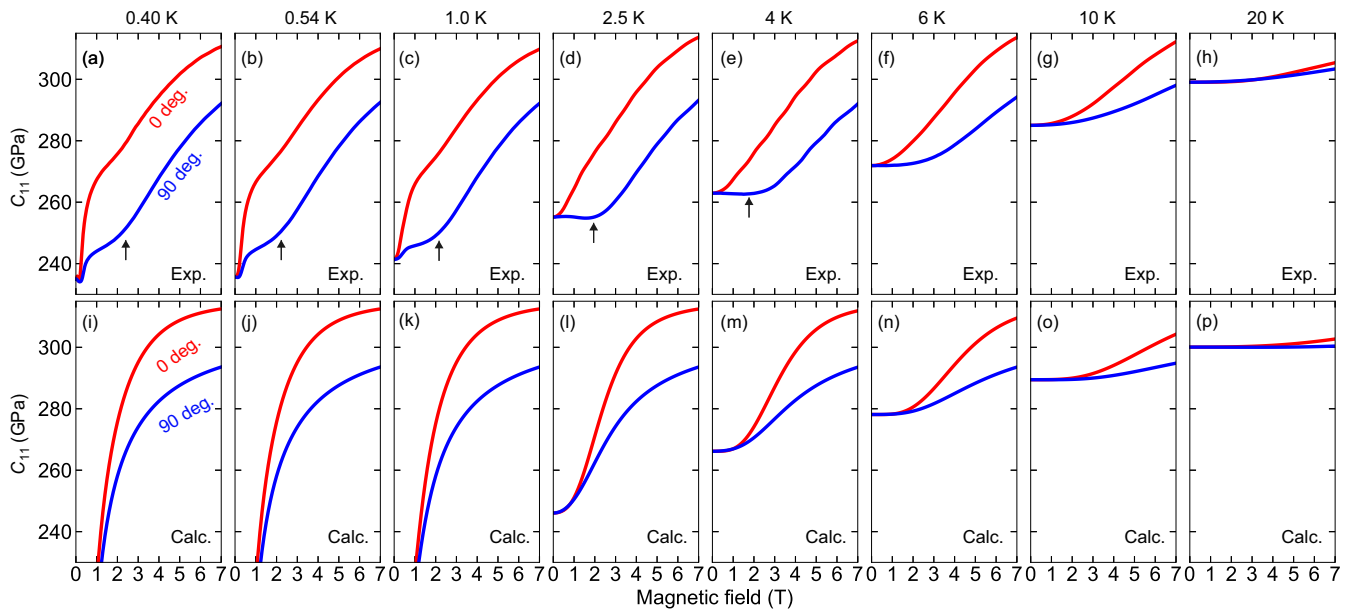


FIG. 2. Magnetic field dependence of (a)–(h) experimental and (i)–(p) calculated elastic constant  $C_{11}(\phi)$  at various temperatures under magnetic field applied parallel ( $\phi = 0^\circ$ ) and perpendicular ( $\phi = 90^\circ$ ) to the propagation direction of ultrasound.

[24], and can be attributable to the quadrupolar ordering transition [23]. As shown in the lower inset of Fig. 1(c), specific heat measurement was also performed at 0 T. The anomaly can be ascribed to the broadened second-order phase transition. Because the specific heat jump corresponds to the transition temperature in a conventional second-order phase transition, the peak temperature in  $-dC/dT$  can be assigned to the transition temperature. It almost corresponds to the kink in  $C_{11}$ . Our specific heat data are similar to that of  $\delta = 0.026$  reported in [37]. On another front, our XRD measurement revealed that  $\delta = 0.012 \pm 0.012$  (see Appendix A for details). Therefore, combining them,  $\delta$  of our sample is considered to be around 0.02. In order to investigate how the quadrupole correlation evolves toward the transition temperature, we have studied the elastic constant  $C_{11}$  in the para-quadrupole state. Figures 2(a)–2(h) show  $C_{11}$  at various temperatures under magnetic field applied parallel ( $\phi = 0^\circ$ ) or perpendicular ( $\phi = 90^\circ$ ) to the propagation direction of ultrasound [see Fig. 1(b) for the definition of  $\phi$ ]. When the magnetic field is applied, the quadrupole fluctuation is suppressed and  $C_{11}$  increases owing to the polarization of magnetic dipole moment. The polarization also induces the anisotropy of the elastic constant. The magnitude of anisotropy is larger in the higher magnetic field and lower temperature. In particular,  $C_{11}$  shows large anisotropy below 4 K;  $C_{11}(\phi = 0^\circ)$  steeply increases with increasing magnetic field, but  $C_{11}(\phi = 90^\circ)$  remains nearly constant below 2 T. Below 1 K, a small cusp was observed for  $\phi = 90^\circ$  in the low magnetic field region. To show the effect of quadrupole correlation, we have performed the calculation of the elastic constant based on a single-ion model as shown in Figs. 2(i)–2(p). In this calculation, CEF, Zeeman field, and the quadrupole-strain coupling were taken into account, while any interaction between  $\text{Tb}^{3+}$  moments was not (the details of the calculation procedure are shown in Appendix B). The difference between the experimental data and the calculation should be ascribed to the correla-

tion effect. The calculated elastic modulus at 0 T diverges toward the zero-temperature following the Curie-type elastic softening [25]. As a result, the elastic constant shows unphysical negative value below 0.45 K. This is partly because higher-order elastic constants and inter-quadrupolar coupling are neglected. Apart from the negative divergence, the calculated  $C_{11}$  of the two orthogonal configurations is almost isotropic below 2 T irrespective of temperature. On the other hand, the experimental elastic constant shows large anisotropy in the low-temperature region while the experiment and the calculation are similar above 10 K. In particular,  $C_{11}$  below 4 K shows gradual kinks as indicated by arrows only for the  $90^\circ$  experimental data. The signatures different from the single-ion calculation seem to be owing to the quadrupole correlation effect.

In order to investigate the elastic anisotropy at low magnetic fields in more detail, we have systematically studied magnetic field angle dependence of  $\Delta C_{11}(\phi) = C_{11}(\phi) - C_{11}(\phi = 0^\circ)$ . We show experimentally measured and calculated angular dependencies under various magnetic fields at a fixed temperature of 4 K in Figs. 3(a) and 3(b), respectively. In a low field, the experimental data of the elastic constant vary with the angle as  $\cos 2\phi$  while the calculation does as  $\cos 4\phi$ . The  $\phi = 0^\circ$  and  $90^\circ$  data are different for the  $\cos 2\phi$  dependence while they are same for the  $\cos 4\phi$  dependence. Therefore, the difference between the experimental and calculation is consistent with that shown in Fig. 2. As the magnetic field is increased, both of the angular dependencies become similar to each other.

Figures 4(a) and 4(b) show experimental and calculated  $\Delta C_{11}(\phi)$  at 1 T for various temperatures. Clear angle dependencies gradually appear upon cooling for both the experimental and calculated data. On the other hand, the main part of experimentally observed angular dependence contains a  $\cos 2\phi$  dependent component while the calculation shows  $\cos 4\phi$  dependence, which is consistent with the results in

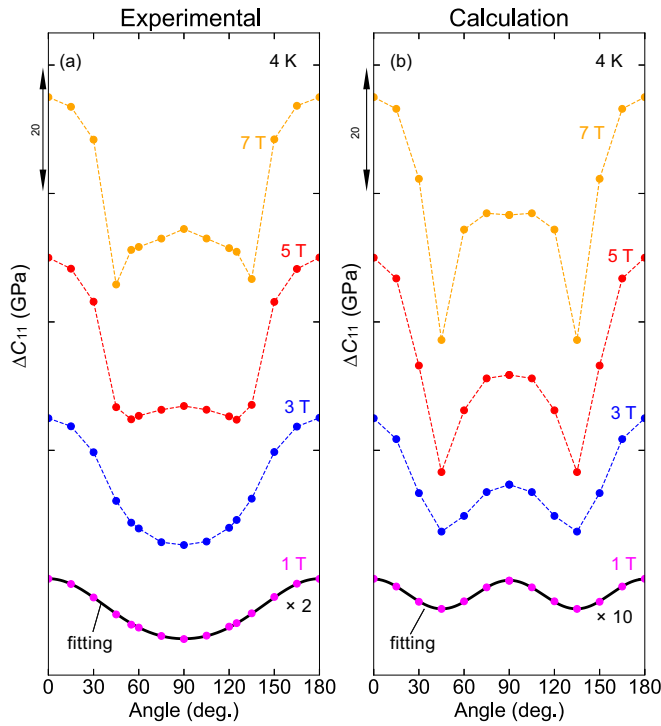


FIG. 3. Magnetic field angle dependence of (a) experimental and (b) calculated  $\Delta C_{11}(\phi)$  under various magnetic fields at 4 K. Magnetic field is rotated with respect to the [100] axis as shown in Fig. 1(b). Data are shown with offset for clarity. Experimental and calculated data at 1 T are multiplied by 2 and 10, respectively. The black solid lines represent fitting curves of  $\Delta C_{11}(\phi) = A_{2\phi} \cos 2\phi + A_{4\phi} \cos 4\phi$  at 1 T.

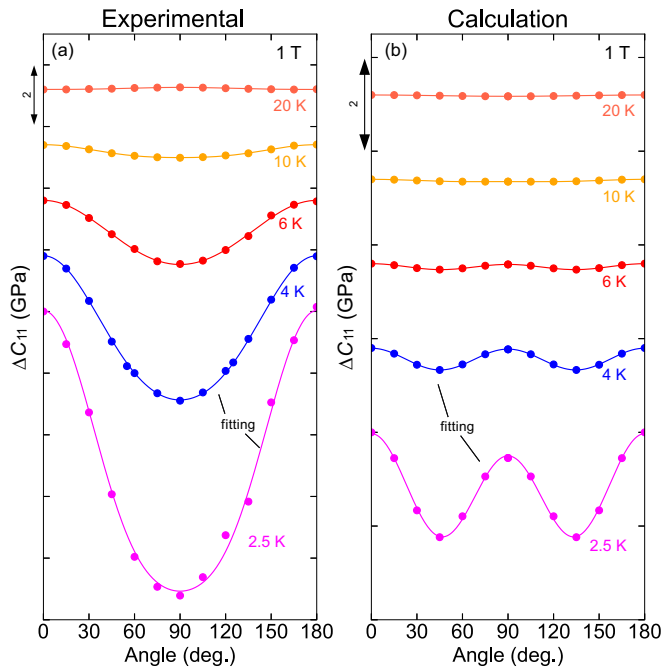


FIG. 4. Magnetic field angle dependence of (a) experimental and (b) calculated  $\Delta C_{11}(\phi)$  at various temperatures. Magnetic field is as large as 1 T and rotated with respect to the [100] axis as shown in Fig. 1(b). Data are shown with offset for clarity. Each solid line represents fitting curves of  $\Delta C_{11}(\phi) = A_{2\phi} \cos 2\phi + A_{4\phi} \cos 4\phi$ .

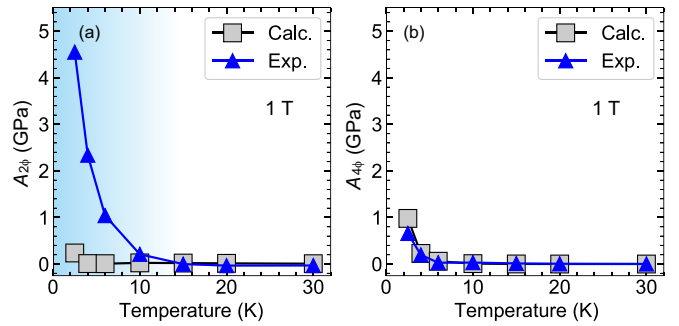


FIG. 5. Temperature dependence of fitting parameters (a)  $A_{2\phi}$  and (b)  $A_{4\phi}$  for the experimental (blue triangle) and the calculation (gray square) at 1 T.

Fig. 3 at low field. Note that this discrepancy does not merely originate from the unoptimized parameters used in our calculation. The  $\cos 2\phi$  dependence cannot be reproduced even when the quadrupolar-strain coupling parameters ( $g_{22}$  and  $g_{yz}$ ) were varied over a wide range. Thus, the  $\cos 2\phi$  dependence can be viewed as a measure of quadrupole correlation, and it is useful to estimate the onset temperature of correlation. To evaluate these angular dependencies, we fitted them by  $\Delta C_{11}(\phi) = A_{2\phi} \cos 2\phi + A_{4\phi} \cos 4\phi$ , where  $A_{2\phi}$  and  $A_{4\phi}$  are fitting parameters at 1 T. Figures 5(a) and 5(b) represent the temperature dependence of these fitting parameters. The most apparent disagreement between experiment and calculation appears in  $A_{2\phi}$  below  $\approx 10$  K. This onset temperature of quadrupole correlation is quite large compared with the quadrupolar-ordering transition temperature of  $\approx 0.4$  K.

To investigate the correlation effect from a different probe, we have measured magnetic field induced strain, i.e., magnetostriction. Complementary to elastic response, magnetostriction probes the quadrupolar moment induced by magnetic field. Figure 6(a) shows magnetostriction measured at various temperatures. Magnetic field was applied along the [001] direction, and the longitudinal ( $e_{zz} \parallel [001]$ ) and the transverse ( $e_{xx} \parallel [100]$ ) strains were measured simultaneously [see Fig. 6(b)]. Being consistent with the previous studies [26,28,29],  $e_{zz}$  is positive while  $e_{xx}$  is negative, and the magnitudes were as large as order of  $10^{-3}$ . As the temperature is decreased, the magnitude of magnetostriction gradually increases. This is reflected by the evolution of magnetic susceptibility. We have also calculated the magnetostrictions for both configurations using the same single-ion model and parameters as in the case of elastic constant (see Appendix B). It well reproduces the experimental data in the high-temperature region, but discrepancy between the experiment and calculation becomes apparent in the low-temperature region below 10 K. This can also be ascribed to the quadrupole correlation effect. To evaluate this discrepancy, the difference between experiment and calculation was exhibited in Fig. 6(c). Similar to the previous case of the elastic constant, it evolves rapidly below around 10 K. The most obvious discrepancy is the magnetostriction perpendicular to the magnetic field; the magnitude of experimental data is almost half of the calculated value. In this direction, the experimental elastic constant is also small compared with the calculation. These discrepancies

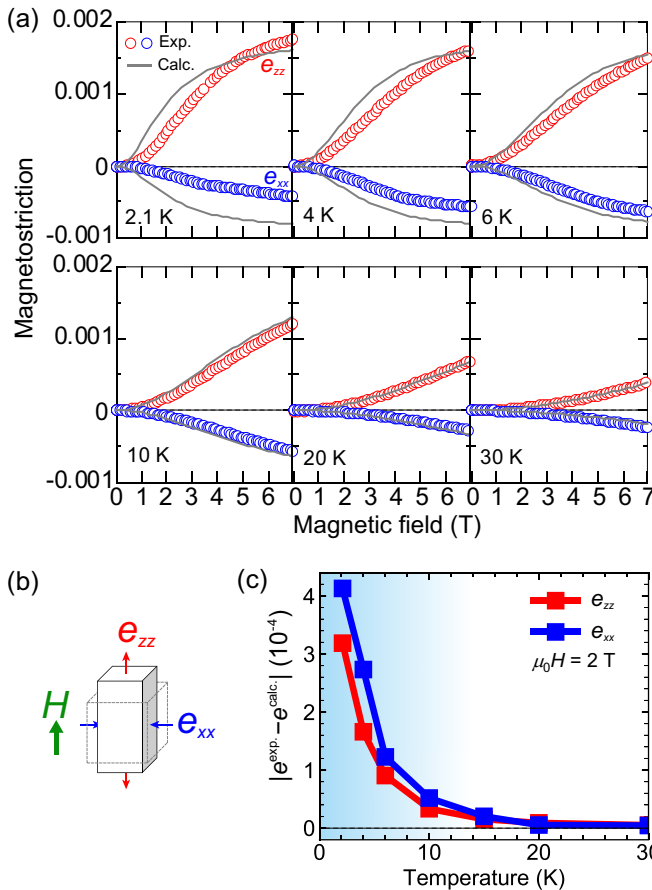


FIG. 6. (a) Magnetostriction at various temperatures.  $e_{zz}$  (red) or  $e_{xx}$  (blue) represents strains parallel or perpendicular to the magnetic field, respectively. The external magnetic field is applied along  $[001]$ . The gray lines represent calculated magnetostriction for both configurations. (b) Experimental configuration of magnetostriction measurements. (c) Difference of magnetostriction between experiment and calculation at a fixed magnetic field of 2 T.

correspond to each other and are considered to be related to quadrupolar correlation.

#### IV. DISCUSSION AND CONCLUSION

In conclusion, we have revealed strong quadrupole correlation in a frustrated quantum magnet  $\text{Tb}_{2+\delta}\text{Ti}_{2-\delta}\text{O}_7$  by means of ultrasound, magnetostriction, and specific heat measurements. Figure 7 summarizes the obtained results. Consistent with the previous reports [23,24], our Tb-rich single crystal showed anomalies of elastic constant and specific heat around 0.4 K, manifesting a long-range quadrupole ordering. We have compared the observed elastic constant and magnetostriction with the calculated data based on a single-ion model. The discrepancy between the observed and calculated data was discerned below about 10 K, indicating breakdown of single-ion picture and strong quadrupole correlation in the paramagnetic state. The onset temperature is far above the long-range quadrupolar ordering temperature of 0.44 K. The magnetic field range of the strong correlation is not clear but supposedly of tesla order judging from the magnetic field dependencies of the elastic constant [Figs. 2(a)–2(e), 3(a)

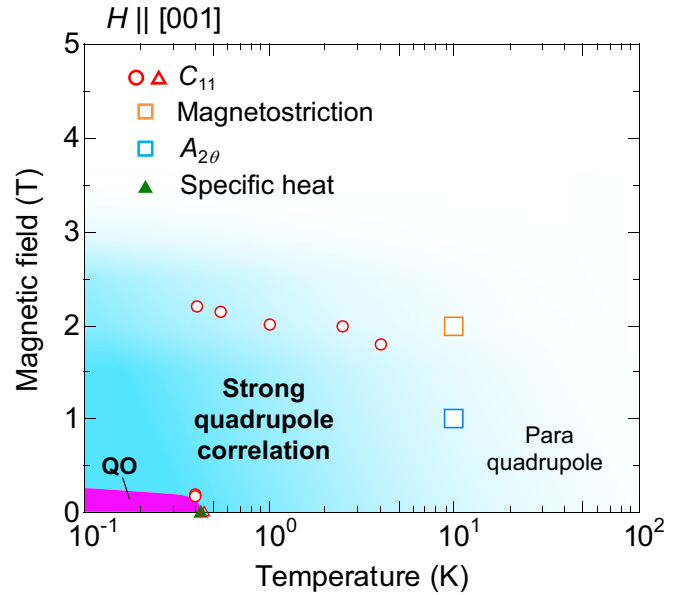


FIG. 7. Phase diagram of  $\text{Tb}_{2+\delta}\text{Ti}_{2-\delta}\text{O}_7$  ( $\delta \approx 0.02$ ). QO stands for a long-range quadrupolar ordered phase. Squares indicate the onset temperature of the quadrupolar correlation determined by  $A_{2\phi}$  and magnetostriction. Red circles represent deflection points of  $C_{11}$  shown by arrows in Figs. 2(a)–2(e). The boundary fields between the strong correlation and induced magnetic state should be larger than them. Red and green triangles correspond to the quadrupolar-ordering temperature determined by the  $C_{11}$  and specific heat shown in Fig. 1(c).

and 3(b)) and magnetostriction [Fig. 6(a)]. In the correlated region, the difference between experiment and calculation was confirmed clearly in the response along the direction perpendicular to the magnetic field. In this direction, the magnetostriction (i.e.,  $e_{xx}$ ) becomes negative and the elastic response (at  $\phi = 90^\circ$ ) remains soft at low magnetic field. These imply that quadrupolar moment tends to avoid the perpendicular direction and quadrupolar fluctuation persists under magnetic field. Although previous theoretical studies took the quadrupole degree of freedom and its correlation into account [6,23], the related magnetoelastic responses were not reported so far. The observations in this study seem useful for the future development of theoretical investigation.

Gritsenko *et al.* estimated a rather small quadrupolar interaction ( $-0.055$  K) based on the Curie-Weiss-like fitting of ultrasound data [24] but such estimation is not accurate even in some simple cases [39]. In fact, several previous studies also suggested the importance of quadrupolar correlation. Klekovkina *et al.* identified the order of magnitude difference between the experimentally observed elastic constants and those calculated based on a single-ion model. They speculated that it is caused by the effect of intersite interaction [36]. Ruff *et al.* observed a substantial broadening of Bragg peaks below 20 K, and attributed it to structural fluctuation caused by the quadrupolar correlation [40]. Inelastic neutron scattering experiments showed that the first excited CEF mode becomes dispersive below about 20 K, suggesting CEF levels among adjacent  $\text{Tb}^{3+}$  ions are interacted [33,41]. Moreover, in a sister compound  $\text{Tb}_2\text{Ge}_2\text{O}_7$ , recent comprehensive study showed

that significant correlations between quadrupolar moments of  $\text{Tb}^{3+}$  ions are present above 1.1 K [42]. These also suggest that the onset of quadrupolar correlation is much higher than the long-range quadrupolar ordering temperature.

The anomalous physical properties in the paramagnetic state such as the giant thermal Hall effect [31,32], magnetoelastic hybrid excitation [33,34], and vibronic state between phonon and CEF states [35] may be related to the effect of quadrupole correlation. While the strong quadrupolar correlation effect persists up to several tens of kelvins, the geometrical frustration seems to suppress the long-range quadrupolar ordering similarly to other pyrochlore systems. The characteristic of  $\text{Tb}_2\text{Ti}_2\text{O}_7$  clarified in this work is that the strong correlation effect shows up in the sector of quadrupole or lattice dynamics. The nature of geometrical frustration effect on the quadrupole degree of freedom is not clear so far. Pioneering theoretical investigations by Khomskii and Mostvov introduced the concept of orbital (i.e., quadrupolar) frustration [43]. This may cause the situation observed in this study. However, there are no established methods that probe quadrupolar frustration, and few experimental investigations are reported [44–46]. Further investigations are needed to clarify the nature of this unexplored but fascinating phenomenon.

#### ACKNOWLEDGMENTS

We are grateful to S. Onoda for fruitful discussions. This work is supported by JSPS KAKENHI (Grants No. JP20K03828 and No. JP21H01036), PRESTO (Grant No. JPMJPR19L6), and the Mitsubishi Foundation.

#### APPENDIX A: ESTIMATION OF THE OFF-STOICHIOMETRIC PARAMETER $\delta$ FROM X-RAY DIFFRACTION

As reported in Refs. [37,38], the off-stoichiometric parameter  $\delta$  of  $\text{Tb}_{2+\delta}\text{Ti}_{2-\delta}\text{O}_7$  is proportional to lattice parameter  $a$ . Thus, precise determination of the lattice parameter allows us to estimate  $\delta$ . Here we performed XRD measurement at 22 °C using a powder sample crushed from a piece of a single crystal. The calibration was also performed using a standard Si powder sample, in which the lattice parameter of  $5.43123 \pm 0.00008$  Å at 22.5 °C [47] and thermal expansion coefficient of  $2.56 \times 10^{-6}$  K<sup>-1</sup> at 293 K [48] were used. By performing least-squares fitting of the Bragg peaks followed by the calibration, we obtained the lattice parameter of the sample at 22 °C to  $10.1539 \pm 0.0015$  Å. Then, using that the thermal expansion coefficient of  $\text{Tb}_2\text{Ti}_2\text{O}_7$  is  $10.3 \times 10^{-6}$  K<sup>-1</sup> at about 280 K [49], the lattice parameter at 26 °C of  $10.1543 \pm 0.0015$  Å was obtained. Finally,  $\delta = 0.012 \pm 0.012$  was deduced according to the relation  $a(\text{Å}, 26^\circ\text{C}) = 0.124418\delta + 10.15280$  [37].

#### APPENDIX B: SINGLE-ION BASED CALCULATION

Here we show the details of calculation for the elastic constant and magnetostriction. This is based on a single-ion model without intersite interaction. As shown in Fig. 8(a),  $\text{Tb}^{3+}$  ions have four inequivalent sites on a pyrochlore lattice. There is no interaction between them in this model. To ob-

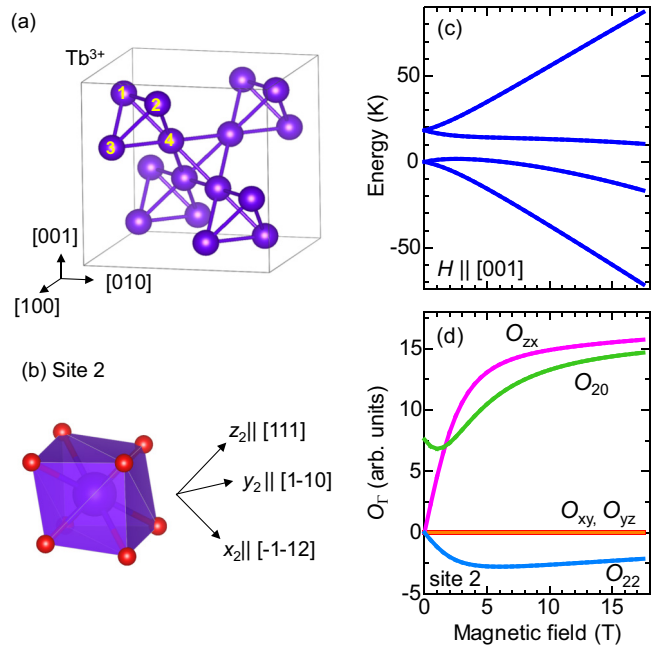


FIG. 8. (a) A schematic of  $\text{Tb}^{3+}$  ions in  $\text{Tb}_2\text{Ti}_2\text{O}_7$  forming pyrochlore lattice. (b) Definition of local crystal axes in a  $\text{TbO}_8$  polyhedron at site 2 in (a). (c) Magnetic field dependence of low-energy CEF levels. The level schemes of every four sites are equivalent when magnetic field is applied along [001]. (d) Magnetic field dependence of electric quadrupole moments at the site 2.

tain the elastic constant and magnetostriction, we separately calculated these quantities for each site and then averaged the four values.

#### 1. Local coordinate

The local coordinates  $(x_m, y_m, z_m)$  of the four sites  $m = 1, 2, 3, 4$  are defined using the global axes as shown in Table I and Figs. 8(a) and 8(b). Using this relation, physical tensors represented by local axes at the  $m$  site can be transformed. For instance, the strain tensors  $e_{ij}^m$  described at a local coordinate  $m$  and the strain tensor  $e_{ij}$  defined in the global frame are transformed by  $e_{\alpha\beta}^m = \sum_{i,j} R_{\alpha i}^m R_{\beta j}^m e_{ij}$ , where the rotation

TABLE I. Correspondence between local orthonormal axes and global cubic axes.  $m$  stands for the four inequivalent  $\text{Tb}^{3+}$  sites shown in Fig. 8(a).

$m$	$x_m$	$y_m$	$z_m$
1	$\frac{1}{\sqrt{6}}(1, 1, 2)$	$\frac{1}{\sqrt{2}}(-1, 1, 0)$	$\frac{1}{\sqrt{3}}(-1, -1, 1)$
2	$\frac{1}{\sqrt{6}}(-1, -1, 2)$	$\frac{1}{\sqrt{2}}(1, -1, 0)$	$\frac{1}{\sqrt{3}}(1, 1, 1)$
3	$\frac{1}{\sqrt{6}}(-1, 1, -2)$	$\frac{1}{\sqrt{2}}(1, 1, 0)$	$\frac{1}{\sqrt{3}}(1, -1, -1)$
4	$\frac{1}{\sqrt{6}}(1, -1, -2)$	$\frac{1}{\sqrt{2}}(-1, -1, 0)$	$\frac{1}{\sqrt{3}}(-1, 1, -1)$

TABLE II. The  $B_{ij}$  parameters used in the present study. The parameters were taken from Ref. [50] and are shown in meV units. In Ref. [50], CEF Hamiltonian is defined as  $\mathcal{H}_{CEF} = \sum_{k,q} \tilde{B}_q^k C_q^k$ , where  $C_q^k$  are Wybourne tensor operators.  $\tilde{B}_q^k$  is converted to  $B_{i,j}$  by using relations of  $B_{20} = \alpha_J \lambda_2^0 \tilde{B}_0^2$ ,  $B_{40} = \beta_J \lambda_2^0 \tilde{B}_4^4$ , and  $B_{60} = \gamma_J \lambda_2^0 \tilde{B}_6^6$ , where  $\alpha_J = -1/99$ ,  $\beta_J = 2/16335$ ,  $\gamma_J = -1/891891$ ,  $\lambda_2^0 = 1/2$ ,  $\lambda_4^0 = 1/8$ ,  $\lambda_4^3 = \sqrt{35}/2$ ,  $\lambda_6^0 = 1/16$ ,  $\lambda_6^3 = \sqrt{105}/8$ , and  $\lambda_6^6 = \sqrt{231}/16$ .

$B_{20}$	$B_{40}$	$B_{43}$
-0.282323	0.00474441	0.0412876
$B_{60}$	$B_{63}$	$B_{66}$
$-4.51288 \times 10^{-6}$	0.000120922	-0.000137393

matrices  $R^m$  are given by

$$R^1 = \begin{pmatrix} \frac{1}{\sqrt{6}} & -\frac{1}{\sqrt{2}} & -\frac{1}{\sqrt{3}} \\ \frac{1}{\sqrt{6}} & \frac{1}{\sqrt{2}} & -\frac{1}{\sqrt{3}} \\ \sqrt{\frac{2}{3}} & 0 & \frac{1}{\sqrt{3}} \end{pmatrix},$$

$$R^2 = \begin{pmatrix} -\frac{1}{\sqrt{6}} & \frac{1}{\sqrt{2}} & \frac{1}{\sqrt{3}} \\ -\frac{1}{\sqrt{6}} & -\frac{1}{\sqrt{2}} & \frac{1}{\sqrt{3}} \\ \sqrt{\frac{2}{3}} & 0 & \frac{1}{\sqrt{3}} \end{pmatrix},$$

$$R^3 = \begin{pmatrix} -\frac{1}{\sqrt{6}} & \frac{1}{\sqrt{2}} & \frac{1}{\sqrt{3}} \\ \frac{1}{\sqrt{6}} & \frac{1}{\sqrt{2}} & -\frac{1}{\sqrt{3}} \\ -\sqrt{\frac{2}{3}} & 0 & -\frac{1}{\sqrt{3}} \end{pmatrix},$$

$$R^4 = \begin{pmatrix} \frac{1}{\sqrt{6}} & -\frac{1}{\sqrt{2}} & -\frac{1}{\sqrt{3}} \\ -\frac{1}{\sqrt{6}} & -\frac{1}{\sqrt{2}} & \frac{1}{\sqrt{3}} \\ -\sqrt{\frac{2}{3}} & 0 & -\frac{1}{\sqrt{3}} \end{pmatrix}.$$

## 2. Hamiltonian

The local Hamiltonian at the  $m$  site ( $m = 1-4$ ) is given by

$$\mathcal{H}^m = \mathcal{H}_{CEF}^m + \mathcal{H}_Z^m + \mathcal{H}_{QS}^m, \quad (\text{B1})$$

where

$$\begin{aligned} \mathcal{H}_{CEF}^m &= B_{20} O_{20}^m + B_{40} O_{40}^m + B_{43} O_{43}^m + B_{60} O_{60}^m \\ &\quad + B_{63} O_{63}^m + B_{66} O_{66}^m, \\ \mathcal{H}_Z^m &= -g_J \mu_B \mu_0 \mathbf{J}^m \cdot \mathbf{H}, \\ \mathcal{H}_{QS}^m &= \sum_{\Gamma} g_{\Gamma} O_{\Gamma}^m e_{\Gamma}^m. \end{aligned} \quad (\text{B2})$$

Here  $\mathcal{H}_{CEF}^m$ ,  $\mathcal{H}_Z^m$ ,  $\mathcal{H}_{QS}^m$  are Hamiltonians representing CEF, Zeeman energy, and quadrupolar-strain coupling, respectively.  $B_{ij}$  and  $O_{ij}^m$  are CEF parameters and the Stevens operators at the  $m$  site. We have taken CEF parameters from Ref. [50] (see Table II).  $g_J = 3/2$ ,  $\mu_B$ ,  $\mu_0$ ,  $\mathbf{J}^m$ , and  $\mathbf{H}$  represent Lande's  $g$  factor, Bohr magneton, permeability in a vacuum, total angular momentum, and magnetic field, respectively.  $O_{\Gamma}^m$ ,  $e_{\Gamma}^m$ , and  $g_{\Gamma}$  are irreducible quadrupolar operator, strain tensor, and the coupling constant belonging to the symmetry  $\Gamma$ , respectively. Here  $\mathbf{J}^m$ ,  $O_{ij}^m$ ,  $O_{\Gamma}^m$ , and  $e_{\Gamma}^m$  are defined in its local frame at the

$m$  site. The explicit form of the Stevens operators is given by [51]

$$\begin{aligned} O_{20}^m &= 3(J_z^m)^2 - J(J+1), \\ O_{40}^m &= 35(J_z^m)^4 - 30J(J+1)(J_z^m)^2 + 25(J_z^m)^2 \\ &\quad - 6J(J+1) + 3J^2(J+1)^2, \\ O_{43}^m &= \{J_z^m [(J_+^m)^3 + (J_-^m)^3] \\ &\quad + [(J_+^m)^3 + (J_-^m)^3] J_z^m\} / 4, \\ O_{60}^m &= 231(J_z^m)^6 - 315J(J+1)(J_z^m)^4 + 735(J_z^m)^4 \\ &\quad + 105J^2(J+1)^2(J_z^m)^2 - 525J(J+1)(J_z^m)^2 \\ &\quad + 294(J_z^m)^2 - 5J^3(J+1)^3 + 40J^2(J+1)^2 \\ &\quad - 60J(J+1), \\ O_{63}^m &= \{[11(J_z^m)^3 - 3J(J+1)J_z^m - 59J_z^m] \\ &\quad \times [(J_+^m)^3 + (J_-^m)^3] + [(J_+^m)^3 + (J_-^m)^3] \\ &\quad \times [11(J_z^m)^3 - 3J(J+1)J_z^m - 59J_z^m]\} / 4, \\ O_{66}^m &= [(J_+^m)^6 + (J_-^m)^6] / 2. \end{aligned}$$

Considering the local  $D_{3d}$  symmetry at the  $\text{Tb}^{3+}$  site,  $\mathcal{H}_{QS}$  can be reduced as

$$\begin{aligned} \mathcal{H}_{QS}^m &= \sum_{\Gamma} g_{\Gamma} O_{\Gamma}^m e_{\Gamma}^m \\ &= g_{20} O_{20}^m e_{20}^m + g_{22} (O_{22}^m e_{22}^m + O_{xy}^m e_{xy}^m) \\ &\quad + g_{yz} (O_{yz}^m e_{yz}^m + O_{zx}^m e_{zx}^m), \end{aligned}$$

where irreducible representations of  $O_{\Gamma}^m$  and  $e_{\Gamma}^m$  are given by

$$\begin{aligned} O_{20}^m &= 3(J_z^m)^2 - J(J+1), \\ O_{22}^m &= [(J_x^m)^2 - (J_y^m)^2] / \sqrt{2}, \\ O_{xy}^m &= (J_x^m J_y^m + J_y^m J_x^m) / \sqrt{2}, \\ O_{yz}^m &= (J_y^m J_z^m + J_z^m J_y^m) / \sqrt{2}, \\ O_{zx}^m &= (J_z^m J_x^m + J_x^m J_z^m) / \sqrt{2}, \\ e_B^m &= e_{xx}^m + e_{yy}^m + e_{zz}^m, \\ e_{20}^m &= (2e_{zz}^m - e_{xx}^m - e_{yy}^m) / 3, \\ e_{22}^m &= (e_{xx}^m - e_{yy}^m) / \sqrt{2}. \end{aligned}$$

By diagonalizing the Hamiltonian shown in Eq. (B1), eigenstates and eigenenergies are obtained. Figure 8(c) shows the obtained eigenenergies as a function of magnetic field. Although only the four CEF levels are represented, all of the thirteen eigenstates are taken into account in the following calculation.

## 3. Elastic constant

To get the magnetoelastic responses, total free energy of  $F = F_{\text{elas}} + F_{\text{elec}}$  is considered [25]. The  $F_{\text{elas}} = \sum_{i,j,k,l} (1/2) C_{ijkl}^0 e_{ij} e_{kl}$  is the elastic part of the free energy and  $F_{\text{elec}} = -(N/\beta) \ln Z$  is the electronic part of the free

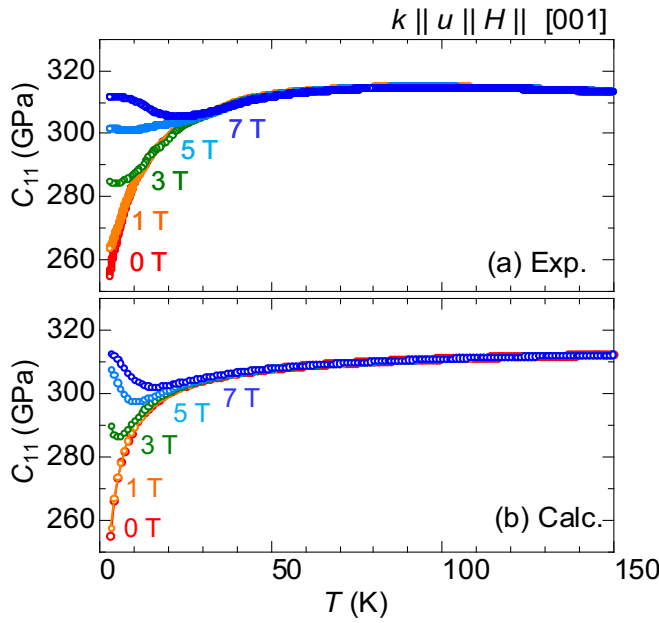


FIG. 9. Temperature dependence of (a) experimental and (b) calculated elastic constants  $C_{11}$  above 2 K at various magnetic fields along [001].

energy. Here  $C_{ijkl}^0$ ,  $N$ , and  $\beta = 1/k_B T$  represent elastic stiffness tensors without electronic contribution, total number of  $\text{Tb}_4$  tetrahedrons in a unit volume, and inverse temperature, respectively.  $Z = \sum_{n,m} e^{-\beta E_{n,m}}$  is the partition function, where  $E_{n,m}$  is the  $n$ th eigenenergy at the  $m$  site. Then  $C_{11}$  is given by taking a second derivative of the total free energy with respect to strain  $e_{zz}$  as [25,36]

$$C_{11} = \frac{\partial^2 F}{\partial e_{zz}^2} = C_{11}^0 - N \sum_{m=1}^4 \sum_{\Gamma} g_{\Gamma} \frac{\partial \langle O_{\Gamma}^m \rangle}{\partial e_{zz}} \left( \frac{\partial e_{\Gamma}^m}{\partial e_{zz}} \right). \quad (\text{B3})$$

The first term is the background elastic constant corresponding to the contribution from the purely elastic energy, and the second term is the modification by the quadrupole-strain coupling. For simplicity,  $C_{11}^0$  is approximated to be constant and temperature independent. The  $\langle O \rangle$  represents the statistical average of the quadrupole moment defined as  $\langle O \rangle = \sum_n \langle n | O | n \rangle e^{-\beta E_n}$ . Here  $|n\rangle$  are the  $n$ th eigenstates. The derivative term  $\partial \langle O_{\Gamma}^m \rangle / \partial e_{zz}$  was approximated to  $(\langle O_{\Gamma}^m \rangle_{\Delta e_{zz}} - \langle O_{\Gamma}^m \rangle_0) / \Delta e_{zz}$ , where  $\Delta e_{zz}$  was set to small finite value of the order of  $10^{-6}$ . The  $\langle O_{\Gamma}^m \rangle_{\Delta e_{zz}}$  and  $\langle O_{\Gamma}^m \rangle_0$  mean  $\langle O_{\Gamma}^m \rangle$  with

and without the small  $\Delta e_{zz}$ . Figure 9 shows comparison of experimental and calculated  $C_{11}$  as a function of temperature. Our calculation reproduces the overall behavior including a broad dip at above 3 T. This supports our calculation and estimated parameters are reasonable.

#### 4. Magnetostriction

By minimizing the free energy with respect to the strain tensors [28,36] (i.e.,  $\partial F / \partial e_{xx} = \partial F / \partial e_{yy} = \partial F / \partial e_{zz} = 0$ ), one gets coupled equations as follows:

$$\begin{aligned} C_{11}^0 e_{xx} + C_{12}^0 (e_{yy} + e_{zz}) &= N \sum_{m=1}^4 \sum_{\Gamma} g_{\Gamma} \langle O_{\Gamma}^m \rangle \left( \frac{\partial e_{\Gamma}^m}{\partial e_{xx}} \right), \\ C_{11}^0 e_{yy} + C_{12}^0 (e_{zz} + e_{xx}) &= N \sum_{m=1}^4 \sum_{\Gamma} g_{\Gamma} \langle O_{\Gamma}^m \rangle \left( \frac{\partial e_{\Gamma}^m}{\partial e_{yy}} \right), \\ C_{11}^0 e_{zz} + C_{12}^0 (e_{xx} + e_{yy}) &= N \sum_{m=1}^4 \sum_{\Gamma} g_{\Gamma} \langle O_{\Gamma}^m \rangle \left( \frac{\partial e_{\Gamma}^m}{\partial e_{zz}} \right). \end{aligned}$$

Then, three strain tensors can be given by

$$\begin{aligned} e_{xx} &= S_0 [(C_{11}^0 + C_{12}^0) \tilde{\sigma}_{xx} - C_{12}^0 (\tilde{\sigma}_{yy} + \tilde{\sigma}_{zz})], \\ e_{yy} &= S_0 [(C_{11}^0 + C_{12}^0) \tilde{\sigma}_{yy} - C_{12}^0 (\tilde{\sigma}_{zz} + \tilde{\sigma}_{xx})], \\ e_{zz} &= S_0 [(C_{11}^0 + C_{12}^0) \tilde{\sigma}_{zz} - C_{12}^0 (\tilde{\sigma}_{xx} + \tilde{\sigma}_{yy})], \end{aligned}$$

where

$$\begin{aligned} S_0 &= [(C_{11}^0)^2 + C_{11}^0 C_{12}^0 - 2(C_{12}^0)^2]^{-1}, \\ \tilde{\sigma}_{ij} &= N \sum_{m=1}^4 \sum_{\Gamma} g_{\Gamma} \langle O_{\Gamma}^m \rangle \left( \frac{\partial e_{\Gamma}^m}{\partial e_{ij}} \right). \end{aligned}$$

Figure 8(d) shows the magnetic field induced evolution of electric quadrupolar moments at  $m = 2$ . Here  $O_{\Gamma} \equiv \langle 0 | O_{\Gamma}^{m=2} | 0 \rangle$  and  $|0\rangle$  represents the lowest CEF level at each magnetic field. The trigonal crystalline field inherent in the pyrochlore systems induces  $O_{20}$  moment even at zero field. The confirmed magnetostriction can be attributable to the magnetically induced local quadrupolar moments of  $O_{20}$ ,  $O_{zx}$ , and  $O_{22}$ .

The best-fitting parameters used in the present calculation are  $C_{11}^0 = 315$  GPa,  $C_{12}^0 = 175$  GPa,  $g_{22} = -80$  K, and  $g_{yz} = 150$  K. The signs of  $g_{22}$  and  $g_{yz}$  are determined from longitudinal and transverse magnetostrictions.  $g_{20}$  cannot be determined since it does not contribute  $C_{11}$ ,  $e_{xx}$ , and  $e_{zz}$ .

[1] P. W. Anderson, *Science* **235**, 1196 (1987).  
[2] L. Balents, *Nature (London)* **464**, 199 (2010).  
[3] A. P. Ramirez, A. Hayashi, R. J. Cava, R. Siddharthan, and B. Shastry, *Nature (London)* **399**, 333 (1999).  
[4] C. Castelnovo, R. Moessner, and S. L. Sondhi, *Nature (London)* **451**, 42 (2008).  
[5] S. Lee, S. Onoda, and L. Balents, *Phys. Rev. B* **86**, 104412 (2012).  
[6] S. Onoda and Y. Tanaka, *Phys. Rev. B* **83**, 094411 (2011).  
[7] L. Savary and L. Balents, *Phys. Rev. Lett.* **108**, 037202 (2012).

[8] J. S. Gardner, M. J. P. Gingras, and J. E. Greedan, *Rev. Mod. Phys.* **82**, 53 (2010).  
[9] M. J. Gingras and P. A. McClarty, *Rep. Prog. Phys.* **77**, 056501 (2014).  
[10] J. G. Rau and M. J. Gingras, *Annu. Rev. Condens. Matter Phys.* **10**, 357 (2019).  
[11] M. J. P. Gingras, B. C. den Hertog, M. Faucher, J. S. Gardner, S. R. Dunsiger, L. J. Chang, B. D. Gaulin, N. P. Raju, and J. E. Greedan, *Phys. Rev. B* **62**, 6496 (2000).  
[12] H. R. Molavian, M. J. P. Gingras, and B. Canals, *Phys. Rev. Lett.* **98**, 157204 (2007).



- [13] J. S. Gardner, S. R. Dunsiger, B. D. Gaulin, M. J. P. Gingras, J. E. Greedan, R. F. Kiefl, M. D. Lumsden, W. A. MacFarlane, N. P. Raju, J. E. Sonier, I. Swainson, and Z. Tun, *Phys. Rev. Lett.* **82**, 1012 (1999).
- [14] J. S. Gardner, A. Keren, G. Ehlers, C. Stock, E. Segal, J. M. Roper, B. Fåk, M. B. Stone, P. R. Hammar, D. H. Reich, and B. D. Gaulin, *Phys. Rev. B* **68**, 180401(R) (2003).
- [15] S. Dunsiger, R. Kiefl, J. Chakhalian, K. Chow, J. Gardner, J. Greedan, W. MacFarlane, R. Miller, G. Morris, A. Price *et al.*, *Phys. B (Amsterdam)* **326**, 475 (2003).
- [16] N. Hamaguchi, T. Matsushita, N. Wada, Y. Yasui, and M. Sato, *Phys. Rev. B* **69**, 132413 (2004).
- [17] J. Gardner, G. Ehlers, S. Bramwell, and B. Gaulin, *J. Phys.: Condens. Matter* **16**, S643 (2004).
- [18] K. C. Rule, J. P. C. Ruff, B. D. Gaulin, S. R. Dunsiger, J. S. Gardner, J. P. Clancy, M. J. Lewis, H. A. Dabkowska, I. Mirebeau, P. Manuel, Y. Qiu, and J. R. D. Copley, *Phys. Rev. Lett.* **96**, 177201 (2006).
- [19] T. Fennell, M. Kenzelmann, B. Roessli, M. K. Haas, and R. J. Cava, *Phys. Rev. Lett.* **109**, 017201 (2012).
- [20] S. Petit, P. Bonville, J. Robert, C. Decorse, and I. Mirebeau, *Phys. Rev. B* **86**, 174403 (2012).
- [21] K. Fritsch, K. A. Ross, Y. Qiu, J. R. D. Copley, T. Guidi, R. I. Bewley, H. A. Dabkowska, and B. D. Gaulin, *Phys. Rev. B* **87**, 094410 (2013).
- [22] H. Kadowaki, M. Wakita, B. Fåk, J. Ollivier, S. Ohira-Kawamura, K. Nakajima, and J. W. Lynn, *Phys. Rev. B* **99**, 014406 (2019).
- [23] H. Takatsu, S. Onoda, S. Kittaka, A. Kasahara, Y. Kono, T. Sakakibara, Y. Kato, B. Fåk, J. Ollivier, J. W. Lynn, T. Taniguchi, M. Wakita, and H. Kadowaki, *Phys. Rev. Lett.* **116**, 217201 (2016).
- [24] Y. Gritsenko, S. Mombetsu, P. T. Cong, T. Stöter, E. L. Green, C. S. Mejia, J. Wosniza, M. Ruminy, T. Fennell, A. A. Zvyagin, S. Zherlitsyn, and M. Kenzelmann, *Phys. Rev. B* **102**, 060403(R) (2020).
- [25] B. Lüthi, *Physical Acoustics in the Solid State* (Springer Science & Business Media, Berlin, New York, 2007).
- [26] L. Mamsurova, K. Pigal'skij, K. Pukhov, N. Trusevich, and L. Shcherbakova, *Zh. Eksp. Teor. Fiz.* **94**, 209 (1988).
- [27] Y. Nakanishi, T. Kumagai, M. Yoshizawa, K. Matsuhira, S. Takagi, and Z. Hiroi, *Phys. Rev. B* **83**, 184434 (2011).
- [28] I. V. Aleksandrov, B. V. Lidskiĭ, L. G. Mamsurova, M. G. Neĭgauz, K. S. Pigal'skiĭ, K. K. Pukhov, N. G. Trusevich, and L. G. Shcherbakova, *Zh. Eksp. Teor. Fiz.* **89**, 2230 (1985).
- [29] J. P. C. Ruff, Z. Islam, J. P. Clancy, K. A. Ross, H. Nojiri, Y. H. Matsuda, H. A. Dabkowska, A. D. Dabkowski, and B. D. Gaulin, *Phys. Rev. Lett.* **105**, 077203 (2010).
- [30] Q. J. Li, Z. Y. Zhao, C. Fan, F. B. Zhang, H. D. Zhou, X. Zhao, and X. F. Sun, *Phys. Rev. B* **87**, 214408 (2013).
- [31] M. Hirschberger, R. Chisnell, Y. S. Lee, and N. P. Ong, *Phys. Rev. Lett.* **115**, 106603 (2015).
- [32] Y. Hirokane, Y. Nii, Y. Tomioka, and Y. Onose, *Phys. Rev. B* **99**, 134419 (2019).
- [33] T. Fennell, M. Kenzelmann, B. Roessli, H. Mutka, J. Ollivier, M. Ruminy, U. Stuhr, O. Zaharko, L. Bovo, A. Cervellino, M. K. Haas, and R. J. Cava, *Phys. Rev. Lett.* **112**, 017203 (2014).
- [34] M. Ruminy, L. Bovo, E. Pomjakushina, M. K. Haas, U. Stuhr, A. Cervellino, R. J. Cava, M. Kenzelmann, and T. Fennell, *Phys. Rev. B* **93**, 144407 (2016).
- [35] E. Constable, R. Ballou, J. Robert, C. Decorse, J.-B. Brubach, P. Roy, E. Lhotel, L. Del-Rey, V. Simonet, S. Petit, and S. de Brion, *Phys. Rev. B* **95**, 020415(R) (2017).
- [36] V. Klekovkina, A. Zakirov, B. Malkin, and L. Kasatkina, *J. Phys.: Conf. Ser.* **324**, 012036 (2011).
- [37] M. Wakita, T. Taniguchi, H. Edamoto, H. Takatsu, and H. Kadowaki, *J. Phys.: Conf. Ser.* **683**, 012023 (2016).
- [38] T. Taniguchi, H. Kadowaki, H. Takatsu, B. Fåk, J. Ollivier, T. Yamazaki, T. J. Sato, H. Yoshizawa, Y. Shimura, T. Sakakibara, T. Hong, K. Goto, L. R. Yaraskavitch, and J. B. Kycia, *Phys. Rev. B* **87**, 060408(R) (2013).
- [39] Even in the molecular field model of a simple two-sublattice antiferromagnet, the estimation is not valid. If the intra-sublattice interaction  $J_F (>0)$  is ferromagnetic and the inter-sublattice interaction  $J_{AF} (<0)$  is antiferromagnetic, the mean-field Néel temperature, which is related to the correlation strength, is governed by the difference of these interactions  $J_F - J_{AF}$  but the Weiss temperature is proportional to the sum  $J_F + J_{AF}$  [52].
- [40] J. P. C. Ruff, B. D. Gaulin, J. P. Castellan, K. C. Rule, J. P. Clancy, J. Rodriguez, and H. A. Dabkowska, *Phys. Rev. Lett.* **99**, 237202 (2007).
- [41] S. Guitteny, J. Robert, P. Bonville, J. Ollivier, C. Decorse, P. Steffens, M. Boehm, H. Mutka, I. Mirebeau, and S. Petit, *Phys. Rev. Lett.* **111**, 087201 (2013).
- [42] A. Hallas, W. Jin, J. Gaudet, E. Tonita, D. Pomaranski, C. Buhariwalla, M. Tachibana, N. Butch, S. Calder, M. Stone *et al.*, [arXiv:2009.05036](https://arxiv.org/abs/2009.05036).
- [43] D. Khomskii and M. Mostovoy, *J. Phys. A* **36**, 9197 (2003).
- [44] F. Reynaud, D. Mertz, F. Celestini, J.-M. Debierre, A. Ghorayeb, P. Simon, A. Stepanov, J. Voiron, and C. Delmas, *Phys. Rev. Lett.* **86**, 3638 (2001).
- [45] V. Fritsch, J. Hemberger, N. Büttgen, E.-W. Scheidt, H.-A. Krug von Nidda, A. Loidl, and V. Tsurkan, *Phys. Rev. Lett.* **92**, 116401 (2004).
- [46] R. Watanuki, G. Sato, K. Suzuki, M. Ishihara, T. Yanagisawa, Y. Nemoto, and T. Goto, *J. Phys. Soc. Jpn.* **74**, 2169 (2005).
- [47] D. L. Kaiser and R. L. Watters, NIST Certificate of SRM 640d, National Institute of Standards and Technology, 2010, [https://www-s.nist.gov/srmors/view\\_cert.cfm?srm=640D](https://www-s.nist.gov/srmors/view_cert.cfm?srm=640D).
- [48] G. White and M. Minges, *Int. J. Thermophys.* **18**, 1269 (1997).
- [49] M. Ruminy, F. Groitl, T. Keller, and T. Fennell, *Phys. Rev. B* **94**, 174406 (2016).
- [50] M. Ruminy, E. Pomjakushina, K. Iida, K. Kamazawa, D. T. Adroja, U. Stuhr, and T. Fennell, *Phys. Rev. B* **94**, 024430 (2016).
- [51] M. T. Hutchings, *Solid State Phys.* **16**, 227 (1964).
- [52] K. Yoshida, *Theory of Magnetism* (Springer-Verlag, Berlin, New York, 1996).